


Article

Moisture Effects on Qualities and Properties of Laser Powder Bed Fusion (LPBF) Additive Manufacturing of As-Built 17-4PH Stainless Steel Parts

Taehwan Kim , Min-Kyeom Kim, Yongjian Fang and Jonghwan Suhr *

Department of Mechanical Engineering, Sungkyunkwan University, 2066 Seobu-ro, Jangan-gu, Suwon-si 16419, Gyeonggi-do, Republic of Korea; kth0116@skku.edu (T.K.); drapix@skku.edu (M.-K.K.); yjfang0507@g.skku.edu (Y.F.)

* Correspondence: suhr@skku.edu

Abstract: Laser powder bed fusion (LPBF) has the advantages of high resolution and geometric freedom but can be susceptible to process failures and defects caused by inappropriate process parameters and powder conditions. This study aims to reveal and quantify the moisture effect on the qualities and properties of as-built parts with various process parameters. The results showed that the density was decreased by 7.86% with humid powder (60.0% relative humidity (RH)) compared to dry powder (3.4%RH). Expectedly, the observed low density led to the property degradation in the hardness, yield strength (YS), and ultimate tensile strength (UTS) of the humid powder by 11.7, 15.02, and 21.25%, respectively, compared to that of dry powder (3.4%RH). Interestingly, the elongation at break of the parts fabricated with humid powder (60.0%RH) was increased by 2.82%, while their YS and UTS were decreased significantly. It seems that the water molecules on the powder surface hindered the reaction between the N₂ shielding gas and melted powder, which resulted in the reduction in the austenite (γ) phase by up to 4.05 wt.%. This could be mainly responsible for the decrease in both the YS and UTS of the humid powder by approximately 100 and 150 MPa, respectively. This study demonstrates that the moisture of the metal powder used for LPBF should be carefully controlled to ensure desirable as-built qualities and properties.



Citation: Kim, T.; Kim, M.-K.; Fang, Y.; Suhr, J. Moisture Effects on Qualities and Properties of Laser Powder Bed Fusion (LPBF) Additive Manufacturing of As-Built 17-4PH Stainless Steel Parts. *Metals* **2023**, *13*, 1550. <https://doi.org/10.3390/met13091550>

Academic Editor: Frank Liou

Received: 9 August 2023

Revised: 25 August 2023

Accepted: 31 August 2023

Published: 3 September 2023



Copyright: © 2023 by the authors. Licensee MDPI, Basel, Switzerland. This article is an open access article distributed under the terms and conditions of the Creative Commons Attribution (CC BY) license (<https://creativecommons.org/licenses/by/4.0/>).

Keywords: laser powder bed fusion; additive manufacturing; moisture content; as-built quality; mechanical properties

1. Introduction

Laser powder bed fusion (LPBF) or selective laser melting (SLM) is one of the additive manufacturing (AM) techniques using a laser or an electron beam to fabricate customized products with a high resolution and complex geometries. However, there are challenges in applying LPBF to various industrial fields such as aerospace, automobile, vessel, and medical fields due to its high level of complexity [1,2]. Initially, LPBF was used to produce prototypes to validate product performance, but LPBF is now capable of producing high-quality products with minimal defects as significant effort is placed on the optimization of process conditions along with the prediction of product quality [3–7].

Despite the developments in LPBF technology, process failures and defects such as cracks, delamination from the substrate, pores, and low quality of the fabrication can still occur due to inappropriate process conditions and powder management [8–11]. To address these limitations, researchers have investigated the effects of the process and powder conditions on the material and mechanical properties of as-built parts [12–14]. It was confirmed that the quality of as-built parts is primarily influenced by the volumetric energy density ($VED = P/(v \cdot l \cdot t)$ (J/mm³)), which is calculated by considering process conditions including the laser power P (W), scan speed v (mm/s), line spacing l (mm), and layer thickness t (mm).

Relative density and material hardness, which significantly affect printing quality, are prone to increase at a higher VED [15–17] and decrease at a lower VED or high scan speed ($v \geq 1300 \text{ mm s}^{-1}$) [9,18]. However, it is observed that both the relative density and hardness of materials are undesirably degraded with the formation of keyhole and gas-entrapped pores at excessively high VEDs [19–21]. Therefore, appropriate process conditions should be determined with VEDs to manufacture as-built parts with minimal pores and high properties [9,15,17,18,22,23]. Additionally, it is important to ensure a lower surface roughness of the as-built parts because it can significantly deteriorate the quality of subsequent layer spreading and also cause defects such as a lack of fusion resulting from the presence of thick powder layers [18]. Typically, an increase in the VED results in improved surface roughness [24]. However, an excessively high VED can have an adverse effect, leading to a decrease in the surface roughness. Therefore, it is essential to determine an appropriate VED by using an ex-characterization method that takes into account the specific process conditions and materials involved. Moreover, some studies have demonstrated that the use of more spherically shaped powders [22] with higher VEDs leads to a higher relative density [9] and ensures a higher yield strength (YS) and ultimate tensile strength (UTS). A reduction in pores resulting from an optimized VED is able to improve mechanical properties [25].

Meanwhile, several studies have noted that the quality of additively manufactured parts can be affected by the conditions of the metal powder, such as the storage conditions, relative humidity (RH), etc. [26]. Grubbs et al. [27] demonstrated that the repeated exposure of metal powder to ambient conditions had negative effects on their flowability. Cordova et al. [28] reported that high moisture in the metal powder can cause agglomeration, low flowability, and low relative density, which can decrease the quality of the manufactured parts and increase the likelihood of process failures. Dutta et al. [29] also noted that the moisture on the powder surfaces could reduce the powder flowability due to capillary effects. Cordova et al. [30] investigated the fact that a high moisture content caused low flowability, a low relative density, and the formation of an oxide film layer due to the absorbance of water molecules on the surface of the metal powder. Hovig et al. [31] found that the moisture and dissolved hydrogen in the powder can affect the formation of hydrogen pores. Furthermore, the mechanical properties of as-built parts fabricated by using recycled powder with high oxygen content could be deteriorated due to the increase in process failures, especially the powder agglomerates and high porosity [32]. Therefore, it can be concluded that using preheated powder could be a methodology to reduce the hydrogen content in the powder.

However, there seems to be no comprehensive investigation of the effects of coupled VEDs with moisture on both the as-built qualities and properties, which can still give rise to challenges in ensuring the as-built qualities even if one of them is optimized. Particularly, compared with other additive manufacturing techniques, such as wire arc additive manufacturing, it is believed that humidity could have a more negative effect on as-built parts fabricated by the LPBF process [33]. To address these issues, this study aims to systematically investigate the effect of powder moisture and VEDs on the as-built qualities of 17-4PH stainless steel parts by evaluating the melt pool dimension, density, and hardness. The as-built microstructures, fabricated by using the dry powder (3.4%RH) and humid powder (60.0%RH), were carefully evaluated through X-ray diffraction (XRD) and energy-dispersive X-ray spectroscopy (EDS). Finally, the tensile properties were characterized and compared by analyzing the microstructures and chemical composition. This study quantitatively analyzed the effects of moisture on the as-built qualities and properties, highlighting that the moisture of metal powder should be managed to guarantee the high printing quality without process failures and defects.

2. Materials and Methods

In this study, 17-4PH stainless steel powders with a density of 7.80 g/cm^3 , supplied by AM Solutions (Uiwang, Republic of Korea), were used with three different moisture

contents: 3.4 (dry powder), 30.0, and 60.0%RH. The dry powder was heated for three days by using a high-temperature furnace supplied by U1TECH (Suwon, Republic of Korea), and the other two types of powder were moisturized to 30.0 and 60.0%RH by using a lab-scale humidity chamber for three days. 17-4PH is a martensitic precipitation-hardening stainless steel exhibiting high strength, corrosion resistance, and toughness [9,18]. The particle size distribution of the 17-4PH powders ranged from 15 to 53 μm in diameter. The chemical composition of the powders in this study is shown in Table 1. The as-built parts were fabricated by SITI-SLM250 and supplied by the Shanghai Industrial Technology Institute (Shanghai, China) with different combinations of laser power (190–400 W), scan speed (250–1000 mm/s), line spacing (80 μm), and layer thickness (40 μm).

Table 1. The chemical composition of 17-4PH stainless steel powder (wt.%).

Material	Fe	C	Cr	Cu	P	Si	Mn	Nb+Ta	Ni	Si
17-4PH	Bal	0.07	15.5–17.5	3.0–5.0	0.03	1.0	1.0	0.15–0.45	3.0–5.0	0.04

2.1. Ex Situ Characterization

Ex situ characterization was conducted by measuring the melt pool characteristics, density, and hardness of the as-built parts. To characterize the melt pool dimension, the cross-section area of the as-built parts was cut in the building direction and observed by an optical microscope (OM, Nikon, Tokyo, Japan) to estimate the melt pool width and depth with different combinations of laser power (190–400 W), scan speed (250–1000 mm/s), line spacing (80 μm), and layer thickness (40 μm). The as-built parts were polished by using a mechanical polisher (GLP Korea, Uiwang, Republic of Korea) with 6 different sandpapers (80, 200, 360, 720, 1200, and 2000 grits) and 1 μm alumina suspension to achieve a mirror-like finish. Finally, the polished samples were etched in an etchant solution (150 mL of H_2O , 25 mL of HNO_3 , 25 mL of HCl , and 1 g of CuCl_2) at room temperature, as shown in Figure 1a.

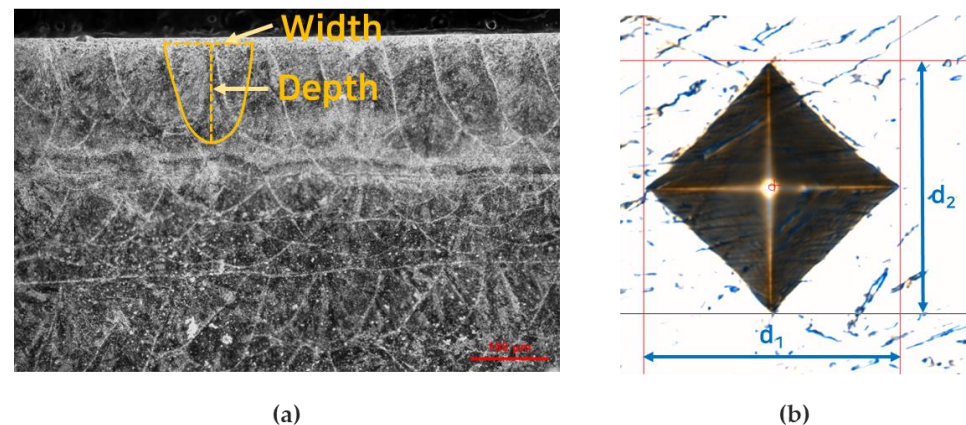


Figure 1. The ex situ characterization of (a) melt pool dimension and (b) Vickers hardness.

Density was measured three times for each part according to the Archimedes principle [34] by using Equation (1):

$$\rho = \rho_{fluid} \cdot \frac{W_{air}}{W_{air} - W_{fluid}} \quad (1)$$

The Vickers hardness was calculated with a 0.5 kgf ($HV_{0.5}$) load and 15 s indentation time, and the width and height were measured by using Leopard 12.0 software (Zootos, Anyang, Republic of Korea) with Equation (2):

$$HV = 1.8544 \frac{F}{\left(\frac{d_1+d_2}{2}\right)^2} \quad (2)$$

where F is the force applied to the diamond in kilogram force and d_1 and d_2 are the dimensions of the indentation, as shown in Figure 1b.

All the experiments for each condition were conducted three times, and we calculated the average of their results.

2.2. Microstructure Characterization

The microstructures of the as-built parts fabricated with dry powder (3.4%RH, DP3.4, Figure 2a) and humid powder (60.0%RH, HP60, Figure 2b) at the determined optimum process condition in Table 2 were characterized by XRD and EDS mapping techniques, respectively. XRD measurements were conducted by SmartLab, supplied by Rigaku (Tokyo, Japan), to evaluate the phase of the as-built parts. The dislocation density difference ($\Delta\rho$) between DP3.4 and HP60 was roughly calculated by using Equation (3) [35]:

$$\Delta\rho = \Delta\beta^2 / (4.35 \times b^2) \quad (3)$$

where $\Delta\beta$ represents the difference in the full width at half maximum (FWHM) of the diffraction peaks and b is the magnitude of the Burgers vector (austenite (γ): 0.256 nm [35]). The as-built parts, with a dimension of $10 \times 10 \times 1.5 \text{ mm}^3$, were prepared for the XRD analysis. The phase fraction of each sample was calculated by using the Rietveld method and MAUD v2.33 [36] software (<https://luttero.github.io/maud/>, accessed on 30 March 2023). The element contents of the as-built parts fabricated with dry powder (3.4%RH, DP3.4) and humid powder (60.0%RH, HP60) were analyzed and compared by using the EDS mapping method by using JSM-IT800 provided by JEOL (Tokyo, Japan).

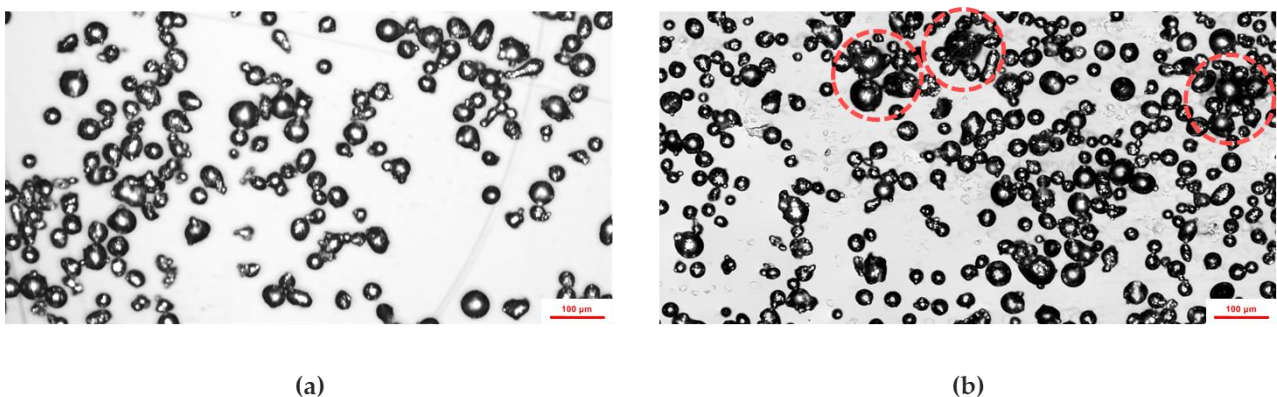


Figure 2. The morphology of (a) dry powder (3.4%RH, DP3.4) and (b) humid powder (60.0%RH, HP60) observed by OM. The dashed red lines indicate the powder agglomerates due to the moisture effect.

Table 2. The optimum process condition of as-built parts (DP3.4 and HP60).

Optimum Process Condition	Laser Power	Scan Speed	Line Spacing	Layer Thickness
	310 W	1000 mm/s	80 μm	40 μm

2.3. Mechanical Properties

After evaluating the ex situ characterization, the optimum process condition which exhibited the greatest material properties was determined for the as-built parts fabricated with three different moisture contents. In order to investigate the effects of moisture on the mechanical properties of the as-built parts, three tensile specimens were fabricated by using the optimum process conditions (Table 2) for DP3.4 and HP60 in accordance with the modified ASTM E8M standards. Tensile tests were conducted by using a Salt-1002 universal testing machine (Salt company, Incheon, Republic of Korea) with a crosshead speed of 0.25 mm min^{-1} . The moisture effects on the mechanical properties were characterized and compared by coupling with the microstructural characteristics.

3. Results and Discussion

3.1. Design of LPBF Process Conditions

3.1.1. Melt Pool Characterization

Table 3 shows whether the as-built parts were fabricated well or failed to print under various combinations of process conditions and three different RHs, as mentioned in Section 2.1. Most of the as-built parts with the higher RH failed to be fabricated because of powder agglomerates during the LPBF process. The melt pool width and depth of the as-built 17-4PH metallic parts are evaluated to determine the melt pool dimension by varying the process conditions including the laser power, scan speed, and RH of the powder. Figure 3 shows that the melt pool width and depth are significantly varied with respect to the laser power and scan speed, indicating that as-built qualities are highly dependent on the VED. It is experimentally observed that a keyhole dominant (Figure 4c) and lack of fusion (Figure 4a) are found when the parts have a VED greater than 100 and less than 60 J/mm^3 , respectively. Note that VED values in between 60 and 100 J/mm^3 are considered to be desirable process conditions (Figure 4b). With the increase in the VED above 100 J/mm^3 , the fused powders can transfer proportionally higher energy to neighboring particles, causing them to melt together [35]. Such conditions resulted in keyhole pores, which increase the melt pool dimension and cause a large denudation zone [37,38]. Additionally, while the melt pool dimension proportionally increases with a higher VED up to a certain point, the dimension decreases with a further increase in the VED, as shown in Figure 3. This is because uneven spreading powders and pores (Figure 4) are caused by spattering and the low surface quality of the previous layer at a high VED ($\geq 100 \text{ J/mm}^3$) [25].

Table 3. The as-built parts and their printing quality with respect to process conditions and three different RHs. A total of $80 \mu\text{m}$ of line spacing and $40 \mu\text{m}$ of layer thickness is used to fabricate as-built parts (O indicates the success of fabrication and X indicates the failure of manufacturing).

No.	Laser Power (W)	Scan Speed (mm/s)	Energy Density (J/mm^3)	%RH (Part Quality)		
1	190	1000	59.375	3.4 (O)	30.0 (O)	60.0 (X)
2	200	1000	62.5	3.4 (O)	30.0 (O)	60.0 (X)
3	210	1000	65.625	3.4 (O)	30.0 (O)	60.0 (X)
4	220	1000	68.75	3.4 (O)	30.0 (O)	60.0 (X)
5	230	1000	71.875	3.4 (O)	30.0 (O)	60.0 (O)
6	240	1000	75	3.4 (O)	30.0 (O)	60.0 (O)
7	250	1000	78.2125	3.4 (O)	30.0 (O)	60.0 (X)
8	260	1000	81.25	3.4 (O)	30.0 (X)	60.0 (X)
9	270	1000	84.375	3.4 (O)	30.0 (O)	60.0 (X)
10	280	1000	87.5	3.4 (O)	30.0 (O)	60.0 (X)

Table 3. Cont.

No.	Laser Power (W)	Scan Speed (mm/s)	Energy Density (J/mm ³)	%RH (Part Quality)		
11	290	1000	90.625	3.4 (O)	30.0 (O)	60.0 (O)
12	300	1000	93.75	3.4 (O)	30.0 (O)	60.0 (O)
13	310	1000	96.875	3.4 (O)	30.0 (O)	60.0 (O)
14	320	1000	100	3.4 (O)	30.0 (O)	60.0 (O)
15	330	1000	103.125	3.4 (O)	30.0 (O)	60.0 (X)
16	340	1000	106.25	3.4 (O)	30.0 (O)	60.0 (X)
17	350	1000	109.375	3.4 (O)	30.0 (O)	60.0 (X)
18	360	1000	112.5	3.4 (O)	30.0 (O)	60.0 (O)
19	370	1000	115.625	3.4 (O)	30.0 (O)	60.0 (O)
20	380	1000	118.75	3.4 (O)	30.0 (O)	60.0 (O)
21	390	1000	121.875	3.4 (O)	30.0 (O)	60.0 (O)
22	400	1000	125	3.4 (O)	30.0 (O)	60.0 (X)
23	200	250	250	3.4 (O)	30.0 (O)	60.0 (X)
24	200	300	208.333	3.4 (O)	30.0 (O)	60.0 (X)
25	200	350	178.571	3.4 (O)	30.0 (O)	60.0 (X)
26	200	400	156.25	3.4 (O)	30.0 (O)	60.0 (X)
27	200	450	138.889	3.4 (O)	30.0 (O)	60.0 (O)
28	200	500	125	3.4 (O)	30.0 (O)	60.0 (O)
29	200	550	113.636	3.4 (O)	30.0 (O)	60.0 (O)
30	200	600	104.167	3.4 (O)	30.0 (X)	60.0 (X)
31	200	650	96.154	3.4 (O)	30.0 (X)	60.0 (X)
32	200	700	89.286	3.4 (O)	30.0 (X)	60.0 (X)
33	200	750	83.333	3.4 (O)	30.0 (X)	60.0 (X)
34	200	800	78.125	3.4 (O)	30.0 (X)	60.0 (X)
35	200	850	73.529	3.4 (O)	30.0 (X)	60.0 (X)
36	200	900	69.444	3.4 (O)	30.0 (X)	60.0 (X)

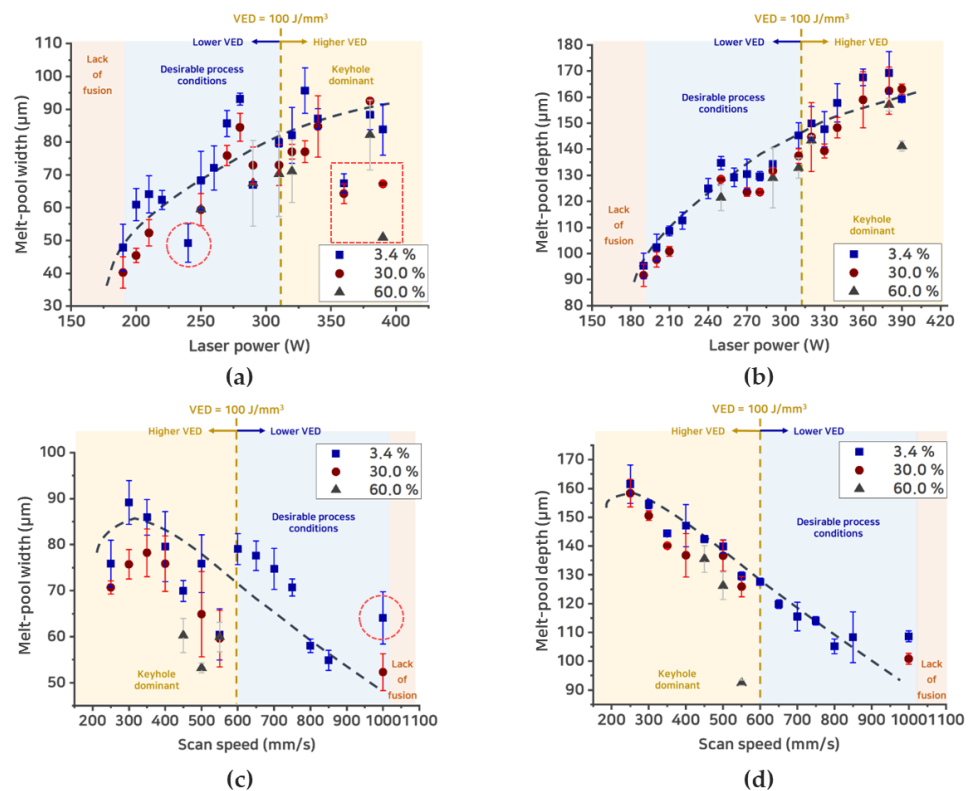


Figure 3. Variations in melt pool width and depth of the as-built parts with three different moisture contents as a function of (a,b) laser power and (c,d) scan speed.

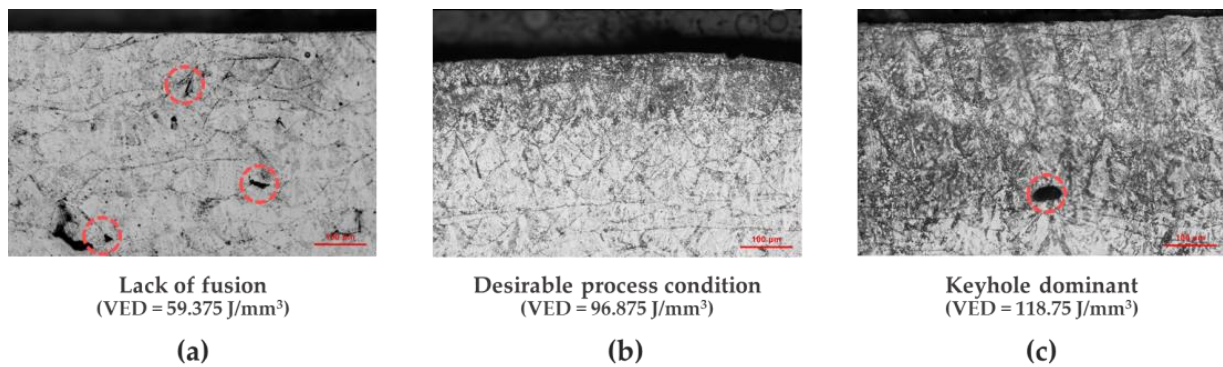


Figure 4. Cross-section images of melt pool with respect to VED: (a) 59.375 J/mm^3 (lack of fusion), (b) 96.875 J/mm^3 (desirable process condition), and (c) 118.75 J/mm^3 (keyhole dominant). The dashed red lines indicate pores generated by each process defect.

However, when a relatively low VED is used to fabricate the as-built parts fabricated with dry powder, a fluctuation in the melt pool width can be found, which is marked by red circles in Figure 3a,c. It is believed that some of the as-built parts fabricated with dry powder under a relatively low VED have pores caused by lack of fusion, which could affect the measurement of the melt pool dimension [10]. For the as-built parts fabricated with humid powder, the fluctuation in the melt pool width can also be observed when a higher VED is used, which is marked by a red rectangle in Figure 3a. This instability could be induced by keyhole phenomena at an excessively high VED [39].

Moreover, it is importantly noted that the melt pool dimension was found to be detrimentally decreased with the addition of moisture. As the RH increases from 3.4% to 60.0%, more and more powder agglomerates (Figure 2b) are observed, which results in the uneven spreading quality and lack of fusion. This can result in a decrease in the density, and most of the as-built parts with humid powders (30.0% and 60.0%RH) are not successfully fabricated at a high scan speed or low laser power (Table 3 and Figure 3c,d). Consequently, compared to the as-built parts with dry powder (3.4%RH), the melt pool width and depth of the as-built parts with humid powder (60.0%RH) are decreased by 0.81% to 25.47% and by 3.79% to 9.85%, respectively, by varying the laser power from 190 to 400 W (Figure 3a,b). Similarly, for the scan speed from 300 to 600 mm/s, the melt pool width and depth of the as-built parts with humid powder are decreased by 0.89% to 29.80% and by 1.96% to 28.65%, respectively (Figure 3c,d). It can be concluded that both the melt pool width and depth are found to be decreased when the as-built part is fabricated with moisture on the 17-4PH powders.

3.1.2. Density

The density of the as-built parts is found to gradually increase with the rising laser power (Figure 5a) and the decreasing scan speed (Figure 5b). However, the density with a high VED over 100 J/mm^3 decreases as a result of the keyholing, which causes entrapped pores (Figure 2) [8,39]. This can lead to a higher porosity inside the as-built parts during the fabrication. It is observed that at a VED of below 60 J/mm^3 , the undesirably developed lack of fusion leads to the small and shallow melt pools inducing the pore formation [10]. Moreover, the powders are not sufficiently melted, causing process failures such as detachment from substrate and recoater crashing.

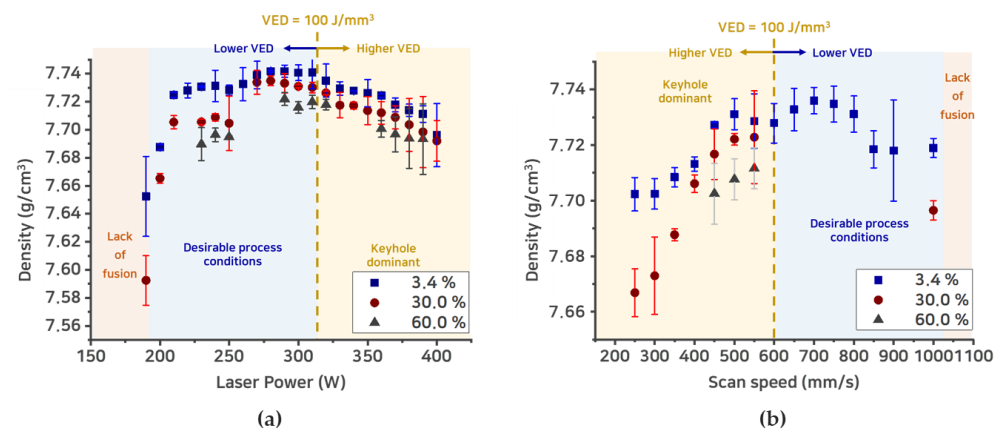


Figure 5. The density of as-built parts with three different moisture contents as a function of (a) laser power and (b) scan speed.

In addition, the decrease in the density of the as-built parts is observed with the increase in moisture, which results in defects induced by the low flowability and poor spreadability of the powders [28]. As the RH increases from 3.4% to 60.0%, compared with the dry powder (3.4%RH), the density of the as-built parts with humid powder (60.0%RH) is decreased by 0.09% to 7.86% under the wide range of the laser power (Figure 5a), whereas that of the as-built parts with humid powder is only decreased by 0.07% to 0.46% under various scan speeds (Figure 5b).

3.1.3. Hardness

The hardness of the as-built parts is characterized by the Vickers hardness test. By varying the laser power from 190 to 400 W, as shown in Figure 6a, the hardness is improved as the VED increases up to 100 J/mm³ while it decreases when the VED is above 100 J/mm³. This is likely because of the formation of the keyhole and gas pores, which would decrease the density [40] and generate a higher stress concentration when the as-built part is compressed by a hardness tester [41]. Similarly, the hardness is increased until the scan speed is increased to 600 mm/s, while it is decreased above 600 mm/s as shown in Figure 6b.

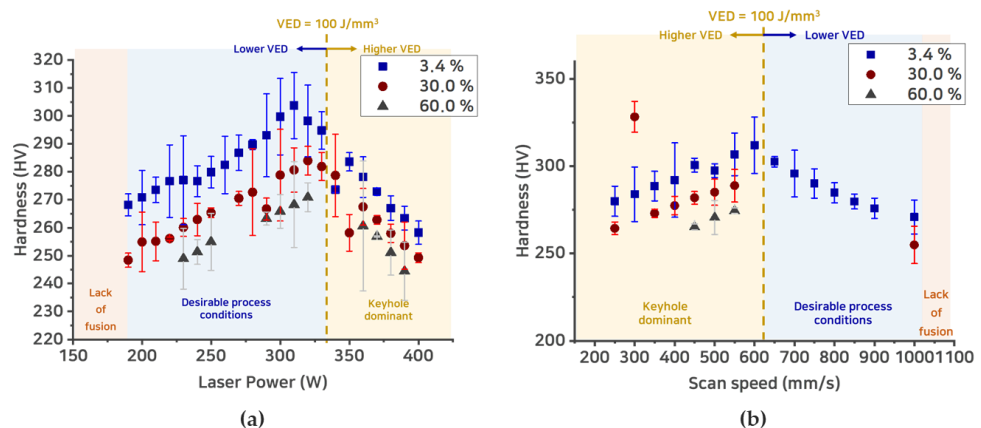


Figure 6. The hardness of as-built parts with three different moisture contents as a function of (a) laser power and (b) scan speed.

Importantly, the decrease in the hardness of the as-built parts with humid powder (60.0%RH) is also evaluated with the increase in moisture. In comparison with the as-built parts with dry powder (3.4%RH), the hardness of the as-built parts with humid powder is decreased by 1.86% to 11.67% in the range of laser powers investigated in this study (Figure 6a) and by 4.15% to 11.75% under various scan speeds (Figure 6b) when the RH of the powders increased from 3.4% to 60.0%. This phenomenon can be interpreted as the

water molecules on the surface of the 17-4PH powders being transformed into hydrogen pores [31] during the LPBF process, and this can induce powder agglomerates with adjacent powders to result in a lack of fusion [42].

Therefore, it can be concluded that it is crucial to control the RH of the powders to avoid process failures such as a lack of fusion [43] and keyhole pores and ensure a high printing quality during the LPBF process of the as-built parts.

3.2. Microstructure Characterization

In order to study the effect of RH on the microstructure of the as-built parts, DP3.4 and HP60 samples are investigated.

From the XRD analysis of DP3.4 and HP60, as shown in Figure 7, the ferrite/martensite (α/α') and γ phases are observed in both DP3.4 and HP60. However, DP3.4 exhibits a higher fraction of the γ phase compared to HP60. The presence of a higher nitrogen (N) content would promote the formation of γ in the as-built parts [44,45]. However, in the case of HP60, water molecules on the powder surface could hinder the reaction between the nitrogen gas and the 17-4PH powders [30]. Consequently, DP3.4 shows a higher fraction of the γ phase by approximately 4.05 wt.%.

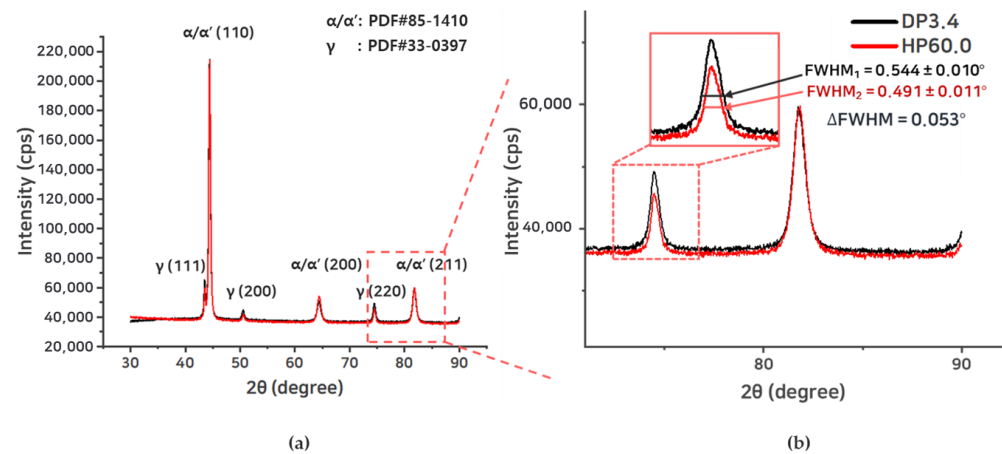


Figure 7. (a) XRD results of DP3.4 and HP60 and (b) a detailed view of peak regions.

The difference in the FWHM of the diffraction peaks of the γ phase, denoted as $\Delta\beta = 0.0538^\circ$ between DP3.4 and HP60, is calculated. The difference in the dislocation density of the γ phase ($\Delta\rho_{aus}$) between DP3.4 and HP60 is determined by using Equation (3), as discussed in Section 2.2.

Furthermore, the results of the EDS analysis (Table 4) show that DP3.4 had higher nitrogen (N) content compared to HP60. This is because when the N_2 shielding gas was used during the LPBF process, the water molecules on the powders in HP60 could cause the formation of oxide film, preventing the reaction of N_2 gas with the 17-4PH powders [30]. Additionally, a higher amount of carbon and nitrogen elements in the DP3.4 specimen (Table 4) could promote the formation of the γ phase through austenitic solidification mode [46] compared to HP60. Consequently, the fraction of the γ phase in DP3.4 was found to be greater than that in HP60 by up to approximately 4.05 wt.%. This higher fraction of the γ phase in DP3.4 can be primarily attributed to the increased carbon and nitrogen elements.

Table 4. EDS mapping results of DP3.4 and HP60 showing chemical compositions of each specimen.

wt.%	C	N	Si	Cr	Mn	Fe	Ni	Cu	Nb
DP3.4	13.7	1.3	0.5	14.3	0.4	60.6	4.0	4.9	0.3
HP60	7.5	0.2	0.7	15.4	0.5	65.3	4.6	5.5	0.3

3.3. Mechanical Properties

The mechanical properties of the DP3.4 and HP60 with the optimum process conditions (Table 2) are characterized by the uniaxial tensile test in terms of the YS (σ_Y), UTS (σ_{UTS}), and elongation at break (ε_{break}). As shown in Figure 8 and Table 5, a large difference in both the YS (~100 MPa) and UTS (~150 MPa) between DP3.4 and HP60 is observed.

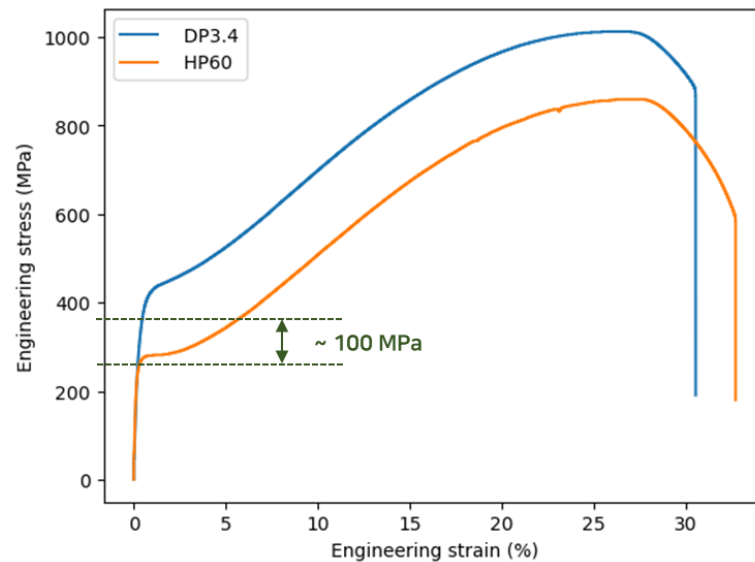


Figure 8. Tensile properties of DP3.4 and HP60. The difference between two dashed lines shows the YS difference between DP3.4 and HP60 calculated by 0.2% strain offset line.

Table 5. Tensile properties with respect to powder conditions.

Samples	σ_Y (MPa)	σ_{UTS} (MPa)	ε_{break} (%)
DP3.4	401.9 ± 8.4	1005.1 ± 18.5	31.32 ± 0.75
HP60	316.5 ± 30.2	854.1 ± 23.1	34.24 ± 1.06

Typically, there are three factors to improve the YS and UTS of DP3.4: a higher dislocation density of the γ phase, stronger solid solution strengthening, and higher γ phase fraction. First, the difference in the dislocation density of the γ phase can contribute to the greater YS observed in DP3.4, as calculated by using Taylor's hardening law in Equation (4) [47]:

$$\sigma_{dis,aus} = M\alpha Gb\Delta\rho_{aus}^{0.5} \quad (4)$$

where $\sigma_{dis,aus}$, M , α , and G are the yield strength contributed by the γ phase dislocations, Taylor factor, constant about the dislocation obstacle efficiency, and shear modulus, respectively [48]. In this case, M is 3.06 [49], α is 0.30 [50], G is 81 GPa [48], and $\Delta\rho_{aus}$ is about $3.092 \times 10^{12} \text{ m}^{-2}$. Therefore, it is understandable that the YS of DP3.4 can be higher than that of HP60 due to the higher dislocation density of the γ phase in DP3.4, as discussed in Section 3.2 (Figure 7), contributing approximately 33.5 MPa to the strength improvement. Second, the more nitrogen elements in DP3.4, as shown in Table 4, can result in the strong solid solution strengthening of interstitial nitrogen atoms, further enhancing the YS and UTS of DP3.4 [51,52].

Finally, the higher fraction of the γ phase in DP3.4 can also, at least in part, contribute to the increase in the UTS, attributed to a higher transformation-induced plasticity (TRIP) effect during deformation [53]. In contrast, HP60 exhibits a lower dislocation density in the γ phase and the weaker solid strengthening of interstitial nitrogen atoms and the TRIP effect due to the detrimental effects of moisture. Consequently, both the YS and UTS of HP60 are decreased by 21.25% and 15.02%, respectively, compared with those of DP3.4.

However, the elongation at break (ϵ_{break}) of HP60 is higher than that of DP3.4 up to 2.82% in Table 5. This might be because the higher dislocation density in DP3.4 can reduce its ability to store additional dislocations, which gives rise to the decrease in the strain hardening rate during deformation [54]. Additionally, the decrease in the ductility of DP3.4 can also be induced by its stronger solid solution strengthening of interstitial nitrogen atoms [55].

4. Conclusions

This study quantitatively investigated the effects of process conditions coupled with moisture on the as-built qualities and properties of 17-4PH stainless steels. With various process parameters, the main defect mechanisms during the LPBF process were observed by ex situ characterization. The keyholing generated entrapped pores with a high VED (≥ 100 J/mm³) while the lack of fusion with a low VED (≤ 60 J/mm³) caused nonmelted powders and process failures.

Additionally, it was noted that the moisture had significant detrimental effects on the as-built qualities and properties under the optimum process condition. The moisture of the 17-4PH powders led to the powder agglomeration, which deteriorated the spreading quality and surface roughness and further contributed to the lack of fusion, pore formation, and process failures. As a result, under the same process conditions, the melt pool width and depth of the as-built parts with humid powder (60.0%RH) were reduced by 1.96% to 28.65% and by 0.81% to 29.80%, respectively, compared with the dry powder. In addition, these reductions in the melt pool dimension resulted in higher surface roughness and internal pores inside the as-built parts. Consequently, the density and hardness of the as-built parts with humid powder (60.0%RH) were reduced by 0.07% to 7.86% and by 1.86% to 11.75%, respectively.

Moreover, the as-built parts with dry powder (3.4%RH) exhibited a higher YS (401.9 MPa) and UTS (1005.1 MPa) compared to that (YS: 316.5 MPa; UTS: 854.1 MPa) of the as-built parts with humid powder (60.0%RH). These differences could be attributed to the difference in the γ fraction (~4.05 wt.%), the solid solution strengthening of the interstitial nitrogen atoms, and the TRIP effect. As a result, the moisture had a negative impact on the mechanical properties of the as-built parts, leading to a 21.25% decrease in the YS and a 15.02% decrease in the UTS but a 2.82% increase in the elongation at break for the as-built parts with humid powder (60.0%RH).

Therefore, this research confirms the crucial role of powder management in conjunction with process optimization for achieving high-quality component fabrication. The insights provided by this work will be valuable for guiding the preparation and manufacturing processes in the context of the LPBF technique.

Author Contributions: Conceptualization, T.K., M.-K.K. and Y.F.; methodology, T.K.; software, T.K.; validation, T.K.; formal analysis, T.K. and Y.F.; investigation, T.K.; resources, J.S.; data curation, T.K.; writing—original draft preparation, T.K.; writing—review and editing, M.-K.K. and J.S.; visualization, T.K.; supervision, J.S.; project administration, J.S.; funding acquisition, J.S. All authors have read and agreed to the published version of the manuscript.

Funding: This work was supported by the National Research Foundation of Korea (NRF) grant funded by the Korea government (MSIT) (No. 2022R1A2C3011968), and the SungKyunKwan University and the BK21 FOUR (Graduate School Innovation) funded by the Ministry of Education (MOE, Korea), and National Research Foundation of Korea (NRF).

Data Availability Statement: The data that support the findings of this study are available from the corresponding author upon reasonable request.

Conflicts of Interest: The authors declare no conflict of interest.

References

1. Campbell, I.; Bourell, D.; Gibson, I. Additive manufacturing: Rapid prototyping comes of age. *Rapid Prototyp. J.* **2012**, *18*, 255–258. [[CrossRef](#)]
2. Khorasani, A.; Gibson, I.; Veetil, J.K.; Ghasemi, A.H. A review of technological improvements in laser-based powder bed fusion of metal printers. *Int. J. Adv. Manuf. Technol.* **2020**, *108*, 191–209. [[CrossRef](#)]
3. Cheng, L.; Liang, X.; Bai, J.; Chen, Q.; Lemon, J.; To, A. On utilizing topology optimization to design support structure to prevent residual stress induced build failure in laser powder bed metal additive manufacturing. *Addit. Manuf.* **2019**, *27*, 290–304. [[CrossRef](#)]
4. Gaikwad, A.; Giera, B.; Guss, G.M.; Forien, J.-B.; Matthews, M.J.; Rao, P. Heterogeneous sensing and scientific machine learning for quality assurance in laser powder bed fusion—A single-track study. *Addit. Manuf.* **2020**, *36*, 101659. [[CrossRef](#)]
5. Scime, L.; Beuth, J. Anomaly detection and classification in a laser powder bed additive manufacturing process using a trained computer vision algorithm. *Addit. Manuf.* **2018**, *19*, 114–126. [[CrossRef](#)]
6. Sutton, A.T.; Kriewall, C.S.; Leu, M.C.; Newkirk, J.W.; Brown, B. Characterization of laser spatter and condensate generated during the selective laser melting of 304L stainless steel powder. *Addit. Manuf.* **2020**, *31*, 100904. [[CrossRef](#)]
7. Sun, W.; Ma, Y.E.; Zhang, W.; Qian, X.; Huang, W.; Wang, Z. Effects of the build direction on mechanical performance of laser powder bed fusion additively manufactured Ti6Al4V under different loadings. *Adv. Eng. Mater.* **2021**, *23*, 2100611. [[CrossRef](#)]
8. Cunningham, R.; Zhao, C.; Parab, N.; Kantzos, C.; Pauza, J.; Fezzaa, K.; Sun, T.; Rollett, A.D. Keyhole threshold and morphology in laser melting revealed by ultrahigh-speed X-ray imaging. *Science* **2019**, *363*, 849–852. [[CrossRef](#)]
9. Hu, Z.; Zhu, H.; Zhang, H.; Zeng, X. Experimental investigation on selective laser melting of 17-4PH stainless steel. *Opt. Laser Technol.* **2017**, *87*, 17–25. [[CrossRef](#)]
10. Tang, M.; Pistorius, P.C.; Beuth, J.L. Prediction of lack-of-fusion porosity for powder bed fusion. *Addit. Manuf.* **2017**, *14*, 39–48. [[CrossRef](#)]
11. Douglas, R.; Lancaster, R.; Jones, T.; Barnard, N.; Adams, J. The Influence of Powder Reuse on the Properties of Laser Powder Bed-Fused Stainless Steel 316L: A Review. *Adv. Eng. Mater.* **2022**, *24*, 2200596. [[CrossRef](#)]
12. Aversa, A.; Lorusso, M.; Trevisan, F.; Ambrosio, E.P.; Calignano, F.; Manfredi, D.; Biamino, S.; Fino, P.; Lombardi, M.; Pavese, M. Effect of process and post-process conditions on the mechanical properties of an A357 alloy produced via laser powder bed fusion. *Metals* **2017**, *7*, 68. [[CrossRef](#)]
13. Letenneur, M.; Kreitchberg, A.; Brailovski, V. Optimization of laser powder bed fusion processing using a combination of melt pool modeling and design of experiment approaches: Density control. *J. Manuf. Mater. Process.* **2019**, *3*, 21. [[CrossRef](#)]
14. Liu, Q.; Wu, H.; Paul, M.J.; He, P.; Peng, Z.; Gludovatz, B.; Kruzic, J.J.; Wang, C.H.; Li, X. Machine-learning assisted laser powder bed fusion process optimization for AlSi10Mg: New microstructure description indices and fracture mechanisms. *Acta Mater.* **2020**, *201*, 316–328. [[CrossRef](#)]
15. Gu, H.; Gong, H.; Pal, D.; Rafi, K.; Starr, T.; Stucker, B. Influences of energy density on porosity and microstructure of selective laser melted 17-4PH stainless steel. In Proceedings of the 2013 International Solid Freeform Fabrication Symposium, Austin, TX, USA, 12–14 August 2013.
16. Suzuki, A.; Nishida, R.; Takata, N.; Kobashi, M.; Kato, M. Design of laser parameters for selectively laser melted maraging steel based on deposited energy density. *Addit. Manuf.* **2019**, *28*, 160–168. [[CrossRef](#)]
17. Tucho, W.M.; Lysne, V.H.; Austbø, H.; Sjolyst-Kverneland, A.; Hansen, V. Investigation of effects of process parameters on microstructure and hardness of SLM manufactured SS316L. *J. Alloys Compd.* **2018**, *740*, 910–925. [[CrossRef](#)]
18. Yang, K.-T.; Kim, M.-K.; Kim, D.; Suhr, J. Investigation of laser powder bed fusion manufacturing and post-processing for surface quality of as-built 17-4PH stainless steel. *Surf. Coat. Technol.* **2021**, *422*, 127492. [[CrossRef](#)]
19. Buhairi, M.A.; Foudzi, F.M.; Jamhari, F.I.; Sulong, A.B.; Radzuan, N.A.M.; Muhamad, N.; Mohamed, I.F.; Azman, A.H.; Harun, W.S.W.; Al-Furjan, M. Review on volumetric energy density: Influence on morphology and mechanical properties of Ti6Al4V manufactured via laser powder bed fusion. *Prog. Addit. Manuf.* **2022**, *8*, 265–283. [[CrossRef](#)]
20. Irrinki, H.; Nath, S.D.; Alhofors, M.; Stitzel, J.; Gulsoy, O.; Atre, S.V. Microstructures, properties, and applications of laser sintered 17-4PH stainless steel. *J. Am. Ceram. Soc.* **2019**, *102*, 5679–5690. [[CrossRef](#)]
21. Liverani, E.; Fortunato, A. Additive manufacturing of AISI 420 stainless steel: Process validation, defect analysis and mechanical characterization in different process and post-process conditions. *Int. J. Adv. Manuf. Technol.* **2021**, *117*, 809–821. [[CrossRef](#)]
22. Brika, S.E.; Letenneur, M.; Dion, C.A.; Brailovski, V. Influence of particle morphology and size distribution on the powder flowability and laser powder bed fusion manufacturability of Ti-6Al-4V alloy. *Addit. Manuf.* **2020**, *31*, 100929. [[CrossRef](#)]
23. Murr, L.E.; Martinez, E.; Hernandez, J.; Collins, S.; Amato, K.N.; Gaytan, S.M.; Shindo, P.W. Microstructures and properties of 17-4 PH stainless steel fabricated by selective laser melting. *J. Mater. Res. Technol.* **2012**, *1*, 167–177. [[CrossRef](#)]
24. Tonelli, L.; Fortunato, A.; Ceschini, L. CoCr alloy processed by Selective Laser Melting (SLM): Effect of Laser Energy Density on microstructure, surface morphology, and hardness. *J. Manuf. Process.* **2020**, *52*, 106–119. [[CrossRef](#)]
25. Yang, T.; Liu, T.; Liao, W.; MacDonald, E.; Wei, H.; Zhang, C.; Chen, X.; Zhang, K. Laser powder bed fusion of AlSi10Mg: Influence of energy intensities on spatter and porosity evolution, microstructure and mechanical properties. *J. Alloys Compd.* **2020**, *849*, 156300. [[CrossRef](#)]
26. Carrion, P.E.; Soltani-Tehrani, A.; Phan, N.; Shamsaei, N. Powder recycling effects on the tensile and fatigue behavior of additively manufactured Ti-6Al-4V parts. *JOM* **2019**, *71*, 963–973. [[CrossRef](#)]

27. Grubbs, J.; Sousa, B.C.; Cote, D. Exploration of the effects of metallic powder handling and storage conditions on flowability and moisture content for additive manufacturing applications. *Metals* **2022**, *12*, 603. [[CrossRef](#)]
28. Cordova, L.; Campos, M.; Tinga, T. Assessment of moisture content and its influence on laser beam melting feedstock. In Proceedings of the Euro PM2017, Milan, Italy, 1–5 October 2017.
29. Dutta, B.; Babu, S.; Jared, B.H. *Science, Technology and Applications of Metals in Additive Manufacturing*; Elsevier: Amsterdam, The Netherlands, 2019.
30. Cordova, L.; Bor, T.; de Smit, M.; Campos, M.; Tinga, T. Measuring the spreadability of pre-treated and moisturized powders for laser powder bed fusion. *Addit. Manuf.* **2020**, *32*, 101082. [[CrossRef](#)]
31. Hovig, E.W.; Holm, H.D.; Sørby, K. Effect of processing parameters on the relative density of AlSi10Mg processed by laser powder bed fusion. In *Advanced Manufacturing and Automation VIII 8*; Springer: Singapore, 2019; pp. 268–276.
32. Popov, V.V., Jr.; Katz-Demyanetz, A.; Garkun, A.; Bamberger, M. The effect of powder recycling on the mechanical properties and microstructure of electron beam melted Ti-6Al-4 V specimens. *Addit. Manuf.* **2018**, *22*, 834–843. [[CrossRef](#)]
33. Martyushev, N.V.; Kozlov, V.N.; Qi, M.; Tynchenko, V.S.; Kononenko, R.V.; Konyukhov, V.Y.; Valuev, D.V. Production of Workpieces from Martensitic Stainless Steel Using Electron-Beam Surfacing and Investigation of Cutting Forces When Milling Workpieces. *Materials* **2023**, *16*, 4529. [[CrossRef](#)]
34. Britannica, E. *The Editors of Encyclopaedia Britannica. de la Enciclopedia Británica*, 2019.
35. Zhang, Y.; Wang, C.; Reddy, K.M.; Li, W.; Wang, X. Study on the deformation mechanism of a high-nitrogen duplex stainless steel with excellent mechanical properties originated from bimodal grain design. *Acta Mater.* **2022**, *226*, 117670. [[CrossRef](#)]
36. Lutterotti, L.; Matthies, S.; Wenk, H.R. MAUD: A friendly Java program for material analysis using diffraction. *IUCr Newsl. CPD* **1999**, *21*, 14–15.
37. Chen, H.; Yan, W. Spattering and denudation in laser powder bed fusion process: Multiphase flow modelling. *Acta Mater.* **2020**, *196*, 154–167. [[CrossRef](#)]
38. Khairallah, S.A.; Anderson, A.T.; Rubenchik, A.; King, W.E. Laser powder-bed fusion additive manufacturing: Physics of complex melt flow and formation mechanisms of pores, spatter, and denudation zones. *Acta Mater.* **2016**, *108*, 36–45. [[CrossRef](#)]
39. Zhao, C.; Parab, N.D.; Li, X.; Fezzaa, K.; Tan, W.; Rollett, A.D.; Sun, T. Critical instability at moving keyhole tip generates porosity in laser melting. *Science* **2020**, *370*, 1080–1086. [[CrossRef](#)]
40. Li, G.; Li, X.; Guo, C.; Zhou, Y.; Tan, Q.; Qu, W.; Li, X.; Hu, X.; Zhang, M.-X.; Zhu, Q. Investigation into the effect of energy density on densification, surface roughness and loss of alloying elements of 7075 aluminium alloy processed by laser powder bed fusion. *Opt. Laser Technol.* **2022**, *147*, 107621. [[CrossRef](#)]
41. Li, G.; Guo, C.; Guo, W.F.; Lu, H.X.; Wen, L.J.; Hu, X.G.; Zhu, Q. Influence of selective laser melting process parameters on densification behavior, surface quality and hardness of 18Ni300 steel. *Key Eng. Mater.* **2020**, *861*, 77–82. [[CrossRef](#)]
42. Riener, K.; Oswald, S.; Winkler, M.; Leichtfried, G.J. Influence of storage conditions and reconditioning of AlSi10Mg powder on the quality of parts produced by laser powder bed fusion (LPBF). *Addit. Manuf.* **2021**, *39*, 101896. [[CrossRef](#)]
43. Bae, J.; Kim, M.-k.; Oh, E.; Yang, K.-T.; Suhr, J. Experimental and numerical investigation of 17–4PH stainless steel fabricated by laser powder bed fusion and hot isostatic pressing. *Mater. Res. Express* **2021**, *8*, 106512. [[CrossRef](#)]
44. Fu, J.; Yang, Y.; Guo, J.; Tong, W. Effect of cooling rate on solidification microstructures in AISI 304 stainless steel. *Mater. Sci. Technol.* **2008**, *24*, 941–944. [[CrossRef](#)]
45. Rajasekhar, K.; Harendranath, C.; Raman, R.; Kulkarni, S. Microstructural evolution during solidification of austenitic stainless steel weld metals: A color metallographic and electron microprobe analysis study. *Mater. Charact.* **1997**, *38*, 53–65. [[CrossRef](#)]
46. Fang, Y.; Zhang, Y.; Kim, M.-K.; Kim, H.-I.; No, J.; Duan, Z.; Yuan, Q.; Suhr, J. An austenite-rich composite of stainless steels with high strength and favorable ductility via selective laser melting of a powder mixture. *Mater. Sci. Eng. A* **2022**, *855*, 143891. [[CrossRef](#)]
47. Estrin, Y. Dislocation-density-related constitutive modeling. *Unified Const. Laws Plast. Deform.* **1996**, *1*, 69–106.
48. Jiang, D.; Gao, X.; Zhu, Y.; Hutchinson, C.; Huang, A. In-situ duplex structure formation and high tensile strength of super duplex stainless steel produced by directed laser deposition. *Mater. Sci. Eng. A* **2022**, *833*, 142557. [[CrossRef](#)]
49. Lee, S.; Estrin, Y.; De Cooman, B.C. Constitutive modeling of the mechanical properties of V-added medium manganese TRIP steel. *Metall. Mater. Trans. A* **2013**, *44*, 3136–3146. [[CrossRef](#)]
50. Xu, J.; Gruber, H.; Boyd, R.; Jiang, S.; Peng, R.L.; Moverare, J.J. On the strengthening and embrittlement mechanisms of an additively manufactured Nickel-base superalloy. *Materialia* **2020**, *10*, 100657. [[CrossRef](#)]
51. Li, H.; Han, Y.; Feng, H.; Zhou, G.; Jiang, Z.; Cai, M.; Li, Y.; Huang, M. Enhanced strength-ductility synergy via high dislocation density-induced strain hardening in nitrogen interstitial CrMnFeCoNi high-entropy alloy. *J. Mater. Sci. Technol.* **2023**, *141*, 184–192. [[CrossRef](#)]
52. Stern, F.; Becker, L.; Cui, C.; Tenkamp, J.; Uhlenwinkel, V.; Steinbacher, M.; Boes, J.; Lentz, J.; Fechte-Heinen, R.; Weber, S. Improving the Defect Tolerance of PBF-LB/M Processed 316L Steel by Increasing the Nitrogen Content. *Adv. Eng. Mater.* **2023**, *25*, 2200751. [[CrossRef](#)]
53. Eskandari, H.; Lashgari, H.; Ye, L.; Eizadjou, M.; Wang, H. Microstructural characterization and mechanical properties of additively manufactured 17–4PH stainless steel. *Mater. Today Commun.* **2022**, *30*, 103075. [[CrossRef](#)]

54. Yang, P.-J.; Li, Q.-J.; Han, W.-Z.; Li, J.; Ma, E. Designing solid solution hardening to retain uniform ductility while quadrupling yield strength. *Acta Mater.* **2019**, *179*, 107–118. [[CrossRef](#)]
55. Kondoh, K.; Issariyapat, A.; Umeda, J.; Visuttipitukul, P. Selective laser-melted titanium materials with nitrogen solid solutions for balanced strength and ductility. *Mater. Sci. Eng. A* **2020**, *790*, 139641. [[CrossRef](#)]

Disclaimer/Publisher's Note: The statements, opinions and data contained in all publications are solely those of the individual author(s) and contributor(s) and not of MDPI and/or the editor(s). MDPI and/or the editor(s) disclaim responsibility for any injury to people or property resulting from any ideas, methods, instructions or products referred to in the content.